



Gas hydrate growth, methane transport, and chloride enrichment at the southern summit of Hydrate Ridge, Cascadia margin off Oregon

M.E. Torres^{a,*}, K. Wallmann^{b,1}, A.M. Tréhu^{a,2}, G. Bohrmann^{c,3},
W.S. Borowski^d, H. Tomaru^e

^aCollege of Oceanic and Atmospheric Sciences, Oregon State University, 104 COAS Admin. Building, Corvallis, OR 97331-5503, United States

^bIFM-GEOMAR Leibniz-Institut für Meereswissenschaften Wischhofstrasse 1-3, D-24148 Kiel, Germany

^cResearch Center Ocean Margins, University of Bremen, Post Box 330 440, D-28334 Bremen, Germany

^dDepartment of Earth Sciences, Eastern Kentucky University, 512 Lancaster Avenue, Roark 103, Richmond, KY 40475-3102, United States

^eDepartment of Earth and Planetary Science, University of Tokyo, Science Building 5, 7-3-1, Hongo Bunkyo-ku, Tokyo 113-0033, Japan

Received 14 January 2004; received in revised form 9 July 2004; accepted 20 July 2004

Editor: E. Boyle

Abstract

At the summit of Hydrate Ridge (ODP Sites 1249 and 1250), pore fluids are highly enriched in dissolved chloride (up to 1370 mM) in a zone that extends from near the sediment surface (~1 mbsf) to depths of 25 ± 5 mbsf. Below this depth, brines give way to chloride values approaching seawater concentrations with lower chloride anomalies superimposed on baseline values. We developed a one dimensional, non-steady state, transport reaction model to simulate the observed chloride enrichment at Site 1249. Our model shows that in order to reach the observed high chloride values, methane must be transported in the gas phase from the depth of the BSR to the seafloor. Methane transport exclusively in the dissolved phase is not enough to form methane hydrate at the rates needed to generate the observed chloride enrichment. Methane transport in the gas phase is consistent with geophysical and logging data, estimates of gas pressure beneath the BSR, and observations of bubble plumes at the seafloor.

In order to reproduce the observed chloride and gas hydrate distributions, the model requires an enhanced rate of hydrate formation in near surface sediments, which we implement through depth-dependent kinetic constants. We argue that this is justified by changes in geomechanical properties of the sediment. At depths shallower than 25 mbsf the force of crystallization can overcome effective overburden stress, and hydrate growth proceeds by particle displacement, thus minimizing capillary inhibition effects.

* Corresponding author. Tel.: +1 541 737 2902; fax: +1 541 737 2064.

E-mail addresses: mtorres@coas.oregonstate.edu (M.E. Torres), kwallmann@ifm-geomar.de (K. Wallmann), trehu@coas.oregonstate.edu (A.M. Tréhu), gbohrmann@uni-bremen.de (G. Bohrmann), borowski@eku.edu (W.S. Borowski), tomaru@eps.s.u-tokyo.ac.jp (H. Tomaru).

¹ Tel.: +49 431 600 2287.

² Tel.: +1 541 737 2655; fax: +1 541 737 2064.

³ Tel.: +49 421 218 8639.

Our calculations indicate the hydrates in the upper sediments of the ridge summit are probably younger than 1500 years, although the age is difficult to constrain. Independent estimates based on seafloor observations at this site yield gas hydrate formation rates at the ridge crest on the order of $10^2 \text{ mol m}^{-2} \text{ year}^{-1}$. These rates are several orders of magnitude higher than those estimated for Site 997 on the Blake Ridge.

© 2004 Elsevier B.V. All rights reserved.

Keywords: methane hydrate; Hydrate Ridge; chloride brine; methane transport

1. Introduction

Methane is an important part of the natural carbon cycle, but much remains unknown about the processes leading to methane generation, its transport and transformations within sediments, and its significance in global carbon budgets [1,2]. Organic-rich sediments at water depths greater than 500 m usually host methane as a clathrate, a frozen compound in which methane and other low molecular weight gases are trapped in a water lattice (e.g., [3]). A large body of information on the nature of these deposits has been

obtained in the last two decades, with significant contributions made by scientific deep sea drilling (see review in [4]). These studies provide thermodynamic constraints on the stability of gas hydrates (e.g., [5–7]) and estimates on the distribution and concentration of methane hydrate worldwide (e.g., [8,9]).

A recent expedition of the Ocean Drilling Program (ODP Leg 204) targeted the gas hydrate deposits on southern Hydrate Ridge, in the Cascadia accretionary margin (Fig. 1) [10]. We conducted the drilling experiments in areas where seafloor processes had been previously investigated (e.g., [11–14]), and

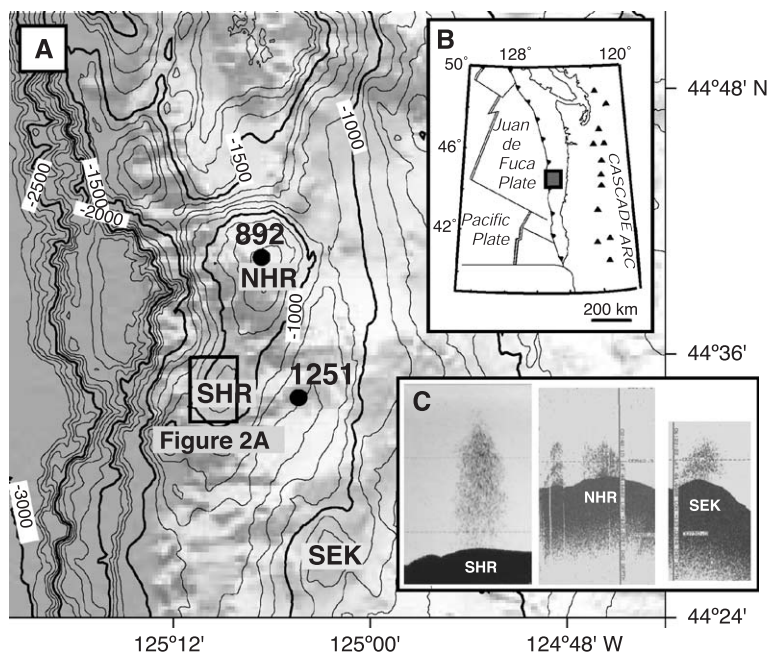


Fig. 1. (A) Regional map of Hydrate Ridge, showing location of Northern Hydrate Ridge (NHR), Southern Hydrate Ridge (SHR) and Southeast Knoll (SEK). Box denotes the area considered in this study (Fig. 2A). Inset B: Tectonic setting of the Cascadia accretionary margin, box shows the location of Hydrate Ridge. (C) Acoustic images of bubble plumes emanating over topographic highs on this margin, consistent with underwater observations. These gas discharge events suggest transport of methane as free gas through the gas hydrate stability zone [13].

where detailed mapping was available [15–17]. The sites drilled during Leg 204 ranged from a depositional basin in which the fluid advection rate is very low (Site 1251, Fig. 1A) to the ridge summit (Sites 1248 to 1250, Fig. 2A), where rapid upward methane transport occurs. Large quantities of gas hydrate were recovered from the uppermost 20 mbsf at Site 1249, consistent with previous TV-guided grab sampling in this area [11–14]. Direct evidence for free gas within the gas hydrate stability zone (GHSZ) was obtained by logging a core recovered at in situ pressure from 14 mbsf at Site 1249 [10,18] and by X-ray computer tomography (CT) studies on near-surface samples (also recovered under pressure) that document the presence of gas-filled pores within hydrate layers [19]. Free gas transport within the GHSZ was previously postulated based on acoustic [13] and submersible [11,20] records of bubble plumes that emerge from

topographic highs on the Oregon slope (Fig. 1C), and has been inferred elsewhere from the presence of bubble plumes, seismic data, and critical pressure models (e.g., [21,22]).

At the ridge summit massive hydrate and free gas coexist with a pore water brine, an unusual occurrence in marine pore waters [4]. Dissolved ions are excluded from the water cages during gas hydrate formation; however, over time, the excluded ions are removed from loci of hydrate formation by advection or diffusion [23]. Gas hydrate dissociation during core recovery typically results in freshening of pore fluids as water sequestered in gas hydrates is released. In a previous study we documented the use of dissolved chloride anomalies, along with other gas hydrate proxies, such as infrared imaging and pressure core data, to constrain the gas hydrate distribution and abundance in the Hydrate Ridge area

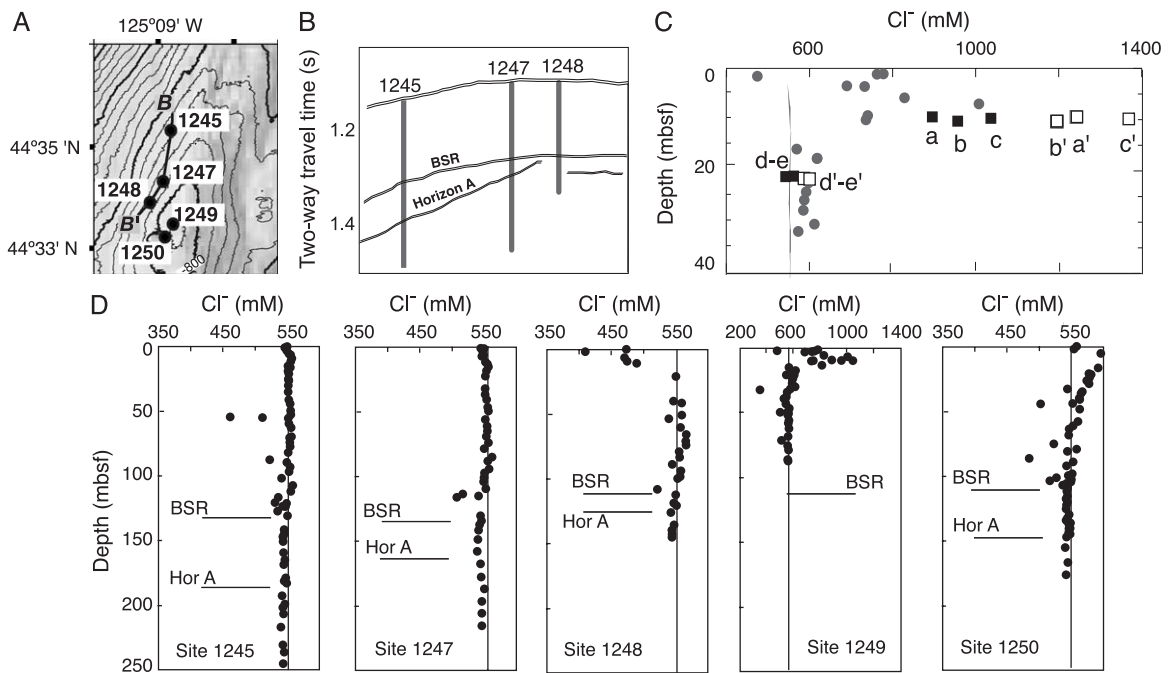


Fig. 2. (A) Detailed bathymetric map [16] showing the locations of ODP sites along a N–S transect towards the ridge summit. (B) Schematic cross section along B–B' Transect (shown in A), illustrating how Horizon A gets shallower towards the summit [10,15]. (C) Chloride data from the upper 40 mbsf of Site 1249 comparing paired samples (denoted by letter and letter prime) collected in an open core from adjacent sediments with different textures. Dry-looking samples (open squares), which did not show texture disruption due to gas hydrate dissociation, have a higher chloride content than samples collected in areas where sediment had liquefied due to gas hydrate dissociation (closed squares). Gray circles are data from whole round samples and fine black line represents data from Site 1245. (D) Chloride concentration in the upper 250 mbsf at sites in the N–S transect in which chloride content beneath the BSR does not show significant deviations from seawater values shown by vertical lines.

[24]. In this paper, we develop a one-dimensional transport-reaction model to simulate the observed chloride enrichment and the mechanisms and time frames needed to produce the observed massive hydrate deposit at Site 1249. Our model shows that the chloride and hydrate distributions at the ridge summit require transport of methane in the gaseous phase from the depth of the bottom simulating reflector (BSR) to the seafloor.

2. Methods and results

Interstitial water samples were obtained on 10- to 20-cm-long whole-round cores that were cut according to ODP protocols [10]. In addition, we obtained pore fluids from sediments sampled on dedicated cores that were split soon after recovery, in an effort to correlate the dissolved chloride concentration with small-scale variations caused by localized dissociation of gas hydrate lenses [24]. Procedures for sample handling and squeezing are detailed in [10]. High-precision chloride concentrations were determined by triplicate titrations using silver nitrate [25]. Chloride measurements are accurate to within 0.4%, and have a standard deviation of 0.2%, based on repeated analyses ($n=28$) of International Association of Physical Sciences Organizations (IAPSO) standard seawater.

The distribution of chloride in pore fluids is shown in Fig. 2, and site location is given in Table 1. The profiles from Sites 1245 and 1247 show background chloride levels that do not deviate significantly from seawater values. Superimposed on this background, discrete negative excursions in the chloride distribution above the BSR reflect heterogeneous distribution of gas hydrate in the

sediment, which average 2% over the GHSZ [24]. In contrast, large amounts of gas hydrate were recovered from shallow sediments at the ridge summit: Sites 1249 and 1250, and to a lesser degree from Site 1248. Pore water from the upper 10 m of sediments at Site 1248 shows chloride concentrations that are significantly lower than seawater values, due to input from the dissociating hydrate. At Sites 1249 and 1250, pore fluids show chloride levels far saltier than the overlying seawater despite fresh water input from hydrate dissociation. This observation supports and greatly extends previous observations of chloride enrichments in the upper 1.2 mbsf [26]. In an effort to recover the most pristine samples that could provide in situ chloride data, we inspected and collected 10 samples from the working half of Cores 204-1249F-3H and -7H, within 90 min of core retrieval. The dissociation of gas hydrate resulted in heterogeneous textures within the core [27]. Some sediment retained its original structure, whereas nearby material had liquefied during gas hydrate dissociation, producing a sediment with a “soupy” appearance. Paired samples (~ 10 cm³ each) were collected from adjacent consolidated and “soupy” sediments for analyses of their chloride content and index properties [27]. In all cases, samples collected from wet-looking sediment indeed have significantly higher water contents and lower chloride concentrations than nearby samples that retained their coherent structure (closed and open squares, respectively, in Fig. 2E). Pore fluids in the dry-looking samples show a [Cl⁻] maximum of 1368 mM at ~ 10 mbsf.

Milkov et al. [18] estimated the in situ salinity of the pore fluids at the ridge summit to be ~ 2105 g kg⁻¹ ([Cl⁻] ~ 1500 mM), which is $\sim 20\%$ higher than our highest measurement. This discrepancy is likely due to

Table 1
ODP Leg 204 sites discussed in this study

Site	Latitude	Longitude	Water depth (mbsf)	Penetration (mbsf)	Depth BSR (mbsf)	Depth Horizon A (mbsf)
1245	44°35.2' N	125°8.9' W	881	540	134	180
1247	44°34.7' N	125°9.1' W	845	220	124	158
1248	44°34.4' N	125°9.1' W	841	149	115	128
1249	44°34.2' N	125°8.8' W	788	90	115	
1250	44°34.1' N	125°9.0' W	807	180	112	150

gas hydrate dissociation during core retrieval. Because all pore water samples are affected by hydrate dissociation, measured chloride concentrations are minimum values.

3. A transport-reaction model for Site 1249

3.1. Transport processes

The model describes changes in dissolved methane and chloride concentrations in pore waters using a one-dimensional, time-dependent transport-reaction scheme that incorporates gas hydrate formation. In this model, dissolved methane and chloride are transported via molecular diffusion and vertical pore water flow. Molecular diffusion coefficients were calculated as a function of temperature using empirical relations given by Boudreau [28]. Diffusion in sediments is also affected by time- and depth-dependent tortuosity (θ), which can be calculated from sediment porosity (Φ) using Archie's law:

$$\theta(z, t)^2 = \Phi(z, t)^{-1} \quad (1)$$

Changes in porosity with depth due to sediment compaction were assumed to follow an empirical exponential function [29],

$$\Phi(z) = \Phi_f + (\Phi_0 - \Phi_f)\exp(-pz) \quad (2)$$

where Φ_f is the porosity at infinite depth, Φ_0 is the porosity at zero depth, p is an attenuation coefficient, and z is sediment depth. The porosity parameter values were determined by fitting function (2) to the measured data [27] as shown in Fig. 3.

In addition to compaction effects, porosity changes over time (t) because of gas hydrate formation. Porosity is calculated as a depth- and time-dependent parameter using the following equation:

$$\Phi(z, t) = \Phi(z) - C_H(z, t) \quad (3)$$

where $\Phi(z)$ is estimated from Eq. (2), and $C_H(z, t)$ is the concentration of gas hydrate expressed as (gas hydrate volume)/(bulk sediment volume).

Active fluid venting at the seafloor has been widely documented at the study site [11–14], thus pore water

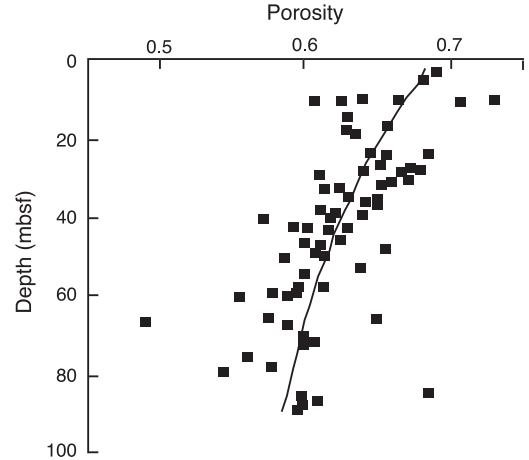


Fig. 3. Porosity data (black squares) from Hole 1249 B and exponential porosity model (solid line) fitted to the data [27] using Eq. (2).

advection from below the GHSZ and through the simulated sediment column has been included in the model. The velocity of water flow (u) is defined as:

$$u(z, t) = \frac{u_0 \Phi_0}{\Phi(z, t)} \quad (4)$$

where u_0 gives the fluid flow rate at the sediment–water interface (zero depth). We used downhole temperatures recorded during Leg 204 to model the vertical fluid advection rate [30,31]. The best fit to the data is for a vertical flow rate of 10 cm year^{-1} (Fig. 4). Alternatively, the data can be fitted with a purely conductive gradient of $0.055 \text{ }^\circ\text{C m}^{-1}$, which is similar to the regional conductive thermal gradient. The estimate of 10 cm year^{-1} thus reflects the upper limit for the rate of fluid advection at this site. These estimates are significantly lower than discharge rate measured at the seafloor [12]. The difference in flow rates reflects the effects of integrating the fluid flow episodicity and the presence of circulation cells, which include a component of seawater flow into the sediment [12].

Solid gas hydrate in the model is buried, assuming that the authigenic hydrates fill the available pore space without expanding the fabric of the sediment or affecting the sedimentation rate. The rate of burial of hydrate and sediment relative to the sediment water interface (v) can then be given by:

$$v(z) = \frac{1 - \Phi_0}{1 - \Phi(z)} v_0 \quad (5)$$

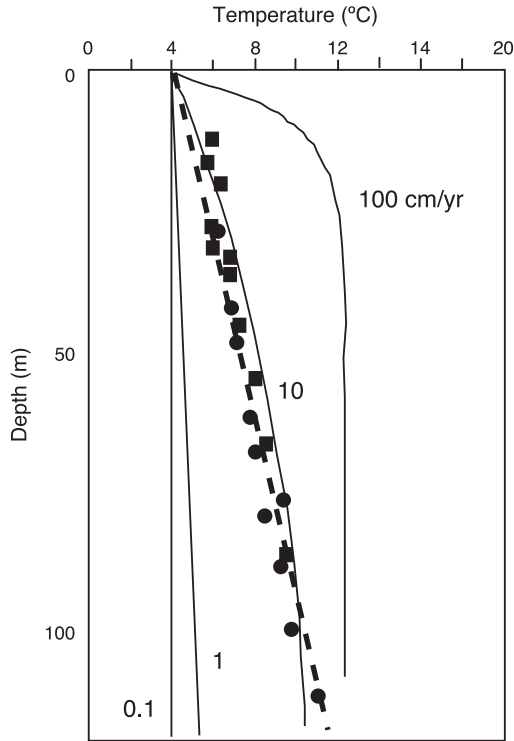


Fig. 4. Downcore temperature data at Sites 1249 (squares) and 1250 (circles), compared to temperatures predicted by a simple model of vertical fluid flow [31] assuming a fluid reservoir temperature of 12.5 °C. Without a conductive gradient, the best fit to the data is for a vertical flow rate of 10 cm year⁻¹ (solid lines); alternatively, the data can be fit with a purely conductive gradient of 0.055 °C m⁻¹ (dashed line). The estimate of 10 cm year⁻¹ reflects the maximum value for the flow rate at this site.

where v_0 is the thickness of the annual layer of sediment deposited with a porosity of Φ_0 .

3.2. Reactions

3.2.1. Thermodynamic constraints

The solubility of methane hydrate ($L_{H(z,t)}$) and the dissolved methane concentration in equilibrium with gas hydrate ($L_{G(z,t)}$) change with depth due to the effects of pressure, temperature and salinity. Using the thermodynamic formulations of Tishchenko et al. [32], we calculated values for $L_{G(z,t)}$ and $L_{H(z,t)}$ as a function of depth and salinity for Site 1249 (Fig. 5). Based on this calculation, the base of the GHSZ is predicted to be at 118 mbsf, which is only 3 m deeper than the estimated depth derived from geophysical data.

3.2.2. Effect of hydrate formation

The rate of change of chloride concentration over time ($R_{Cl}=dC_{Cl}/dt$) and the rate of gas hydrate formation (R_H) are related as shown in Eq. (6) (for derivation, see [33]).

$$R_{Cl}(z, t) = \frac{dC_{Cl}(z, t)}{dt} = \frac{C_{Cl}(z, t)\rho_{gh}R_H(z, t)}{\rho_{pw}\Phi(z, t) - \rho_{gh}d\Phi_{gh}}$$

$$= \frac{C_{Cl}(z, t)\rho_{gh}}{\rho_{pw}\Phi(z, t)}R_H(z, t) \quad (6)$$

where ρ_{gh} and ρ_{pw} represent the density of gas hydrate and pore water, respectively (Table 2), and $\Phi(z,t)$ represents sediment porosity as given by Eq. (3). Gas hydrate precipitation is governed by the saturation state of the solution with respect to solid

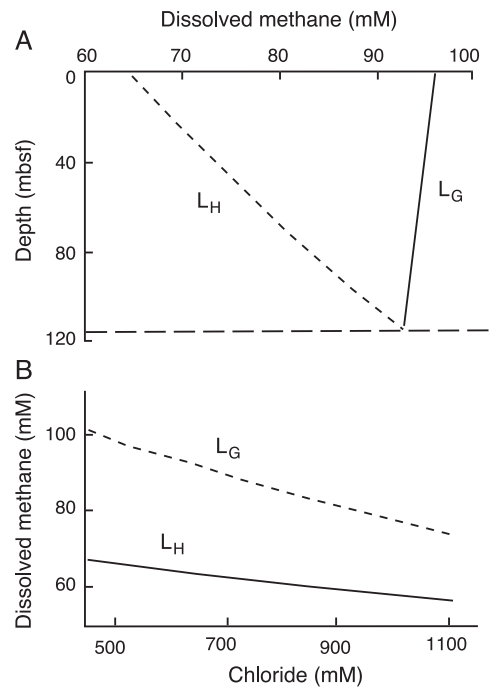


Fig. 5. Thermodynamic equilibria for methane in aqueous, gas and gas hydrate at Site 1249, based on algorithms of Tishchenko et al. [32]. We assumed conditions prevailing at the sediment/water interface on Hydrate Ridge: bottom water temperature of 4.3 °C; geothermal gradient of 0.049 °C m⁻¹; water depth of 778 m at the sediment–water interface and hydrostatic pressure at depth. (A) Change in solubility of gas hydrate (L_H) and methane gas (L_G) with sediment depth. (B) Effect of salinity on the solubility of pure methane gas hydrate (L_H) and methane gas (L_G).

Table 2
Parameter values applied in the model

Parameter	Symbol	Value
Initial porosity at zero depth (seafloor)	Φ_0	0.687
Initial porosity at infinite depth	Φ_f	0.542
Attenuation coefficient	p	$1.4 \times 10^{-4} \text{ cm}^{-1}$
Density of pore water	ρ_{pw}	1.03 g cm^{-3}
Density of gas hydrate	ρ_{gh}	0.9 g cm^{-3}
Molecular weight of gas hydrate	M_{GH}	122.3 g mol^{-1}
Fluid flow rate at zero depth (seafloor)	u_0	$0-10 \text{ cm year}^{-1}$
Burial rate at zero depth (seafloor)	v_0	$0.015 \text{ cm year}^{-1}$
Kinetic constant for gas hydrate precipitation	k_{H}	$0.01 \text{ to } 1 \mu\text{mol cm}^{-3} \text{ year}^{-1}$
Kinetic constant for gas bubble dissolution	k_{G}	$0 \text{ to } 400 \text{ year}^{-1}$
Methane concentration at zero depth (seafloor)	C_{M}^0	0 mM
Methane concentration at depth L	C_{M}^{L}	93 mM
Chloride concentration at zero depth (seafloor)	C_{Cl}^0	558 mM
Chloride concentration at depth L	C_{Cl}^{L}	558 mM
Length of model column	L	11,800 cm
Integration time	t	1 to 25000 year
Phase pressure of hydrate ($r=0.5 \mu\text{m}$)	P_{h}	120 kPa
Phase pressure of gas hydrate ($r=0.5 \mu\text{m}$)	P_{g}	280 kPa

In cases where parameters are varied among various model runs, here we list the ranges used and the specific values are listed in Table 3.

hydrate. Here we express hydrate growth based on transition state theory [34], defined as:

$$R_{\text{H}}(z, t) = k_{\text{H}} \left(\frac{C_{\text{M}}(z, t)}{L_{\text{H}}(z, t)} - 1 \right) \quad (7)$$

where k_{H} is the kinetic constant for hydrate formation, $C_{\text{M}}(z, t)$ is the dissolved methane concentration and $L_{\text{H}}(z, t)$ is the methane concentration in equilibrium with gas hydrate (Fig. 5A). Gas hydrate dissolution is not considered in the model and is inhibited using a Heaviside function.

Methane for gas hydrate formation within the GHSZ is supplied by advection of either methane-enriched pore fluids, or free gas, or both. To generate the most comprehensive model, we allow for both mechanisms

in our formulation, and ran the model for various scenarios, including methane transfer exclusively from the dissolved phase and methane transfer from saturated fluids plus free gas. Methane transfer from pore fluid advection is controlled by the methane solubility (L_{H}) and the velocity of upward fluid flow (u). Methane transfer from the gas phase can be expressed by:

$$R_{\text{G}}(z, t) = k_{\text{G}}(L_{\text{G}}(z, t) - C_{\text{M}}(z, t)) \quad (8)$$

where k_{G} is the kinetic constant for gas dissolution (Table 2). In the model, gas hydrate precipitates rapidly so that the methane concentration in the fluid is always very close to its saturation concentration with respect to gas hydrate. The rate of methane consumption (R_{M}) [in units of $\mu\text{mol methane (cm}^3 \text{ pore water)}^{-1} \text{ year}^{-1}$] is related to the hydrate formation rate (R_{H}) [in $\text{cm}^3 \text{ hydrate (cm}^3 \text{ bulk sediment)}^{-1} \text{ year}^{-1}$] by:

$$R_{\text{M}}(z, t) = 10^6 \frac{\rho_{\text{gh}}}{M_{\text{GH}}} \frac{R_{\text{H}}(z, t)}{\Theta(z, t)} \quad (9)$$

where M_{GH} is the molecular weight of gas hydrate (Table 2).

3.3. Equations

The changes in dissolved methane and chloride (C_{Cl} and C_{M}) and the change in the gas hydrate content (C_{G}) can be described by the following coupled differential equations that express the concentration changes in terms of diffusion, advection and reaction terms, such that:

$$\begin{aligned} \frac{\partial}{\partial t}(\Phi(z, t) \cdot C_{\text{Cl}}(z, t)) = & \frac{\partial}{\partial z} \left(\Phi(z, t) \cdot \frac{D_{\text{Cl}}}{\Theta(z, t)^2} \cdot \frac{\partial C_{\text{Cl}}(z, t)}{\partial z} \right. \\ & \left. + \Phi(z, t) \cdot u(z, t) \cdot C_{\text{Cl}}(z, t) \right) \\ & + \Phi(z, t) \cdot R_{\text{Cl}}(z, t) \end{aligned} \quad (10)$$

$$\begin{aligned} \frac{\partial}{\partial t}(\Phi(z, t) \cdot C_{\text{M}}(z, t)) = & \frac{\partial}{\partial z} \left(\Phi(z, t) \cdot \frac{D_{\text{M}}}{\Theta(z, t)^2} \cdot \frac{\partial C_{\text{M}}(z, t)}{\partial z} \right. \\ & \left. + \Phi(z, t) \cdot u(z, t) \cdot C_{\text{M}}(z, t) \right) \\ & + \Phi(z, t) \cdot (R_{\text{G}}(z, t) - R_{\text{M}}(z, t)) \end{aligned} \quad (11)$$

$$\frac{\partial}{\partial t}(C_G(z, t)) = \frac{\partial}{\partial z}(-v(z, t) \cdot C_G(z, t)) + R_G(z, t) \quad (12)$$

where C_{Cl} and C_M are given in $\mu\text{mol}/\text{cm}^3$ pore water and C_G is given in cm^3/cm^3 bulk sediment. Inserting the constitutive equations defined above, the differential equations are simplified to:

$$\begin{aligned} \frac{\partial}{\partial t}(\Phi(z, t) \cdot C_{Cl}(z, t)) &= \frac{\partial}{\partial z} \left(\Phi(z, t)^2 \cdot D_{Cl} \cdot \frac{\partial C_{Cl}(z, t)}{\partial z} \right. \\ &\quad \left. + \Phi_0 \cdot u_0 \cdot C_{Cl}(z, t) r \right) + C_{Cl}(z, t) \\ &\quad \cdot \frac{\rho_{gh}}{\rho_{pw}} \cdot R_H(z, t) \end{aligned} \quad (13)$$

$$\begin{aligned} \frac{\partial}{\partial t}(\Phi(z, t) \cdot C_M(z, t)) &= \frac{\partial}{\partial z} \left(\Phi(z, t)^2 \cdot D_M \cdot \frac{\partial C_M(z, t)}{\partial z} \right. \\ &\quad \left. + \Phi_0 \cdot u_0 \cdot C_M(z, t) \right) + \Phi(z, t) \\ &\quad \times (R_G(z, t) - R_M(z, t)) \end{aligned} \quad (14)$$

$$\frac{\partial}{\partial t}(C_G(z, t)) = \frac{\partial}{\partial z} \left(-\frac{1 - \Phi_0}{1 - \Phi(z)} \cdot v_0 \cdot C_G(z, t) \right) + R_G(z, t) \quad (15)$$

Since the vertical distribution of gas hydrate is described by a first order differential equation (Eq. (15)), only one boundary condition has to be defined. Here, we apply:

$$\frac{\partial C_C(L, t)}{\partial x} = 0 \quad (16)$$

where L defines the depth to the base of the model column, which is situated at the bottom of the GHSZ. At Site 1249, we define $L=118$ mbsf, based on thermodynamic estimates.

Second order differential equations are used to describe the concentration changes of dissolved

chloride and methane, so that two boundary conditions have to be applied for each:

$$C_{Cl}(0, t) = C_{Cl}^0 \quad C_{Cl}(L, t) = C_{Cl}^L \quad (17)$$

$$C_M(0, t) = C_M^0 \quad C_M(L, t) = C_M^L \quad (18)$$

The chloride concentrations are set to the ambient seawater values ($C_{Cl}=558$ mM) both at the sediment/water interface ($z=0$) and at the bottom of the GHSZ ($z=L$) (Fig. 2). The methane concentration is set to zero at $z=0$. This assumption is supported by repeated measurements of dissolved methane content in the pore fluids in the immediate vicinity of vent sites, which never exceeded $30 \mu\text{M}$ [11,35]. The methane concentration is assumed to be saturated with methane at the bottom of the GHSZ ($C_M=93$ mM), based on thermodynamic algorithms [32]. With these boundary conditions, the model was run for three different scenarios. In the first case, the methane supplied to the system is limited to that in the dissolved phase, which is constrained by methane solubility (Fig. 5). In the second scenario, methane is supplied by a mixture of dissolved methane and free methane gas, assuming a constant value for the kinetic constant for gas dissolution. Finally, a third scenario is shown in which the kinetic constants for hydrate formation and rate of methane transfer from the gas phase are allowed to vary with depth.

3.4. Scenario 1: Methane supplied exclusively as a dissolved phase

In a first series of model runs, methane transfer from gas (k_G) in Eqs. (13)–(15) was set to zero as no free gas is allowed within the GHSZ. Gas hydrate formation was simulated from rising fluids that were saturated with methane at the base of the GHSZ. Upon ascent, the fluids lose dissolved methane because methane solubility decreases with decreasing depth (Fig. 5A). The methane concentrations are maintained close to saturation because the chosen value for the hydrate precipitation kinetic constant ($k_H=0.01 \mu\text{mol cm}^{-3} \text{ year}^{-1}$) is sufficiently large to remove methane, in an approach analogous to that used in [36] and [37]. This assumption is supported by experimental data

obtained in deep-sea environments and in the laboratory, which document that kinetic effects at negligible confining stresses are not a limiting factor in the formation of gas hydrate [38,39]. Fluid flow rates were allowed to vary from 1 to 10 cm/year (Table 3), as constrained by downcore temperature data (Fig. 4). When the model was run using flow velocities of 1 cm/year, dissolved chloride and methane values approached steady state after 15,000 years. For flow velocities of 10 cm/year, steady state for the dissolved species was reached after integration times of 1500 years.

In this scenario, gas hydrate concentration increases with depth to ~7% vol. (Fig. 6). Chloride

Table 3

Values for parameters used in the model runs in each of the three scenarios, results of which are illustrated by solid, dashed and dotted lines in Figs. 6–8

Scenario 1—Fig. 6			
Parameter	Units	Solid line	Dashed line
k_G	(year ⁻¹)	0	0
k_H	($\mu\text{mol cm}^{-3} \text{ year}^{-1}$)	0.01	0.01
u_0	(cm year ⁻¹)	10	1
t	(years)	25,000	25,000

Scenario 2—Fig. 7

Parameter	Units	Solid line	Long dash	Short dash
k_G	(year ⁻¹)	0.1	0.1	0.1
k_H	($\mu\text{mol cm}^{-3} \text{ year}^{-1}$)	0.01	0.01	0.01
u_0	(cm year ⁻¹)	10	1	0
t	(years)	750	1000	

Scenario 3A—Fig. 8A

Parameter	Units	Solid line	Dashed line
k_G^B	(year ⁻¹)	Eq. (19)	Eq. (19)
k_G^{MAX}	(year ⁻¹)	1	10^{-3}
k_G	(year ⁻¹)	400	0.4
k_H	($\mu\text{mol cm}^{-3} \text{ year}^{-1}$)	0.01	0.01
u_0	(cm year ⁻¹)	1	1
t	(years)	1	1000

Scenario 3B—Fig. 8B

Parameter	Units	Solid line	Dashed line
k_G	(year ⁻¹)	0.1	1
k_H	($\mu\text{mol cm}^{-3} \text{ year}^{-1}$)	Eq. (20)	Eq. (20)
u_0	(cm year ⁻¹)	1	1
t	(years)	1500	150

Symbols are defined in Table 2.

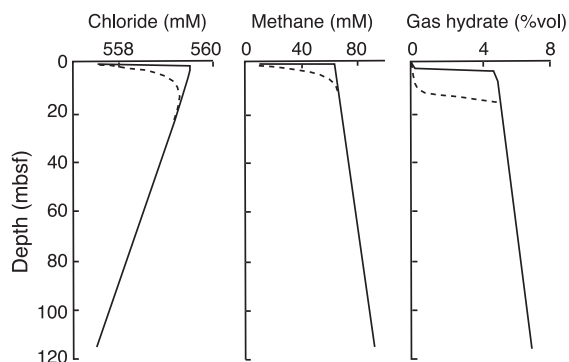


Fig. 6. Results of model runs for a system where methane is transported exclusively by the advecting fluids (i.e., without allowing for methane gas transport and dissolution, $k_G=0$), calculated for flow velocities of 1 (dashed line) and 10 (solid curves) cm year⁻¹. Other model conditions are given in Table 3. Note that in this scenario it is not possible to achieve the observed chloride enrichment.

concentrations increase linearly with decreasing sediment depth due to the continued precipitation of gas hydrate and coeval salt exclusion. However, the resulting chloride enrichments are very small (<600 mM). Because of its low solubility, the methane needed for massive gas hydrate formation requires fluid transport at rates significantly higher than 10 cm/year, in which case the excluded chloride would be rapidly flushed out of the system with the advecting fluids, thus precluding brine formation.

3.5. Scenario 2: Methane supplied by a mixture of gas-saturated fluids and free gas

In a second set of model runs, a mixture of a methane-saturated fluid and free gas is allowed to move towards the sediment surface. Dissolved methane is continuously removed from the solution via gas hydrate precipitation while methane gas is allowed to dissolve in the rising fluids according to the prevailing solubility. Through this approach, the rates of hydrate precipitation are greatly enhanced because methane is delivered continuously from an extensive gaseous pool. For simplicity, we assume that enough gas is available so that hydrate precipitation is not restricted by the gas supply, and it is only limited by the rate constants of gas dissolution and hydrate precipitation.

Due to the high rates of hydrate formation, the porosity of the sediment changes rapidly over time. As the diffusion and advection rates depend on porosity, a full steady state was not attained. The first simulation with $u_0=10$ cm year⁻¹ was terminated after 750 years of integration time and simulations with $u_0=1$ cm year⁻¹ were terminated after 1000 years of integration time (Table 3), when dissolved chloride concentrations reach measured values (Fig. 7). Chloride concentrations using low flow rates are much higher than the values produced using $u_0=10$ cm year⁻¹, because the lower velocity of upward fluid flow reduces the flushing of the pore space with deep fluids of ambient salinity. The dissolved methane concentrations do not depend on the fluid flow velocity because the high value of the kinetic constant for hydrate precipitation maintained the methane concentrations always close to the saturation values.

At the end of the integration times, gas hydrate occupies 15% to 20% of the total volume of near-surface sediments (Fig. 7). The resulting gas hydrate concentrations are larger in the run using lower flow rates because in this case ($u_0=1$ cm year⁻¹) the model was run for a longer time. The rate of gas dissolution depends on the solubility contrast between methane gas and gas hydrates ($L_G(z,t) - C_M(z,t)$); where C_M is kept at saturation values due to high rates of hydrate precipitation. Because of the depth-dependent contrast between L_G and L_H (Fig. 5), the rate of gas dissolution is high in the near-

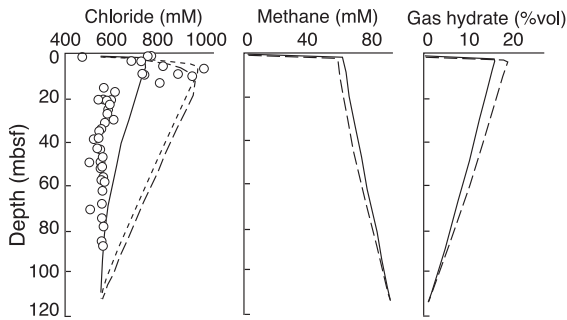


Fig. 7. Dissolved chloride and methane concentrations and gas hydrate contents calculated for three different flow velocities considering gas transport and dissolution ($k_G=0.1$ year⁻¹). The rate of upward fluid flow (u_0) was set at 0 (short-dash line), 1 (long-dash line) and 10 cm year⁻¹(solid line) (Table 3). Chloride concentrations measured in the pore fluids recovered from Site 1249 are indicated as open circles.

surface sediments, which cause a rapid transfer of methane from the gas phase into solution and then into solid gas hydrates. The dissolved chloride concentrations are greatly enhanced relative to scenario 1, due to the high rates of gas hydrate formation. The shape of the profile reflects high rates of gas hydrate formation near the sediment surface and continuous accumulation of chloride in the rising fluids.

3.6. Scenario 3: Kinetic constants vary with depth

Scenario 2 reproduces the upward increase in gas hydrate towards the seafloor (Fig. 7), validating our premise that vertical gas ascent is needed to produce the strong chloride and gas hydrate enrichments at this site. However, it does not explain the strong and selective chloride and gas hydrate enrichment in the top 25 ± 5 m of the sediment column. We postulate that processes driving enhanced rates of hydrate formation in the near surface are controlled by the decrease in effective overburden pressure in shallow sediments relative to deeper sequences (see Section 3.7). Thus, we ran a third series of simulations using enhanced rates of gas dissolution and hydrate precipitation near the sediment surface.

In scenario 3A, we allowed the kinetic constant for gas bubble dissolution (k_G) to vary with sediment depth using the following pulse function:

$$k_G = k_G^B + k_G^{MAX}(e^{-0.2z}) \quad (19)$$

where the parameter k_G^{MAX} defines a maximum value for k_G , reached at 3.5 mbsf, and k_G^B gives the low k_G value at the base of the GHSZ. The value of 3.5 mbsf was chosen because at shallower depths the dissolved methane concentration deviates from its saturation values due to diffusion to the overlying seawater (Fig. 6). We are aware, however, that any values for k_G^B and k_G^{MAX} are very uncertain, so we ran the model using two values for these parameters that differ by several orders of magnitude. In the first case (solid lines in Fig. 8A), using k_G^B and k_G^{MAX} values of 1 and 400 year⁻¹, and a flow velocity of 1 cm year⁻¹, the predicted chloride values approach measured concentrations after only 1 year of integration time, and

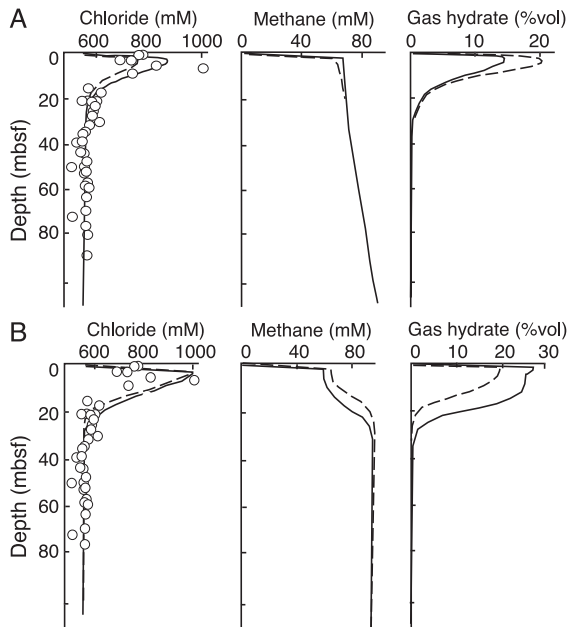


Fig. 8. Dissolved chloride, methane, and gas hydrate concentrations calculated for two different scenarios using enhanced gas dissolution and hydrate precipitation rates in near-surface sediments, where effective stress of the sediment is lower than the internal pressure of a gas bubble and hydrate crystallite. Conditions for each run are listed in Table 3. Chloride concentrations measured in the pore fluids from Site 1249 are indicated as open squares. (A) Results for scenario 3A, in which k_G is allowed to change with depth in two simulation runs. In both simulations, flow velocity was assumed to be 1 cm year^{-1} , and the kinetic constant for hydrate precipitation was kept constant ($k_H=0.01 \text{ } \mu\text{mol cm}^{-3} \text{ year}^{-1}$). Solid lines show results using values for the kinetic constant for gas dissolution at 3.5 mbsf ($k_G^{\text{MAX}}=400 \text{ year}^{-1}$), and at 115 mbsf ($k_G^{\text{B}}=1 \text{ year}^{-1}$), and an integration time of 1 year. Broken lines show results using values for the kinetic constant for gas dissolution at 3.5 mbsf ($k_G^{\text{MAX}}=0.4 \text{ year}^{-1}$), and at 115 mbsf ($k_G^{\text{B}}=0.001 \text{ year}^{-1}$), and an integration time of 1000 year. (B) Results for scenario 3B, in which the kinetic constant for gas precipitation is allowed to vary with depth. Flow velocity is assumed to be 1 cm year^{-1} . Solid lines depict results of the model run for 1500 years, using a value of k_G of 0.1 year^{-1} ; dashed lines shows results of integrations over 150 years applying k_G of 1 year^{-1} . Both scenarios (3A and 3B) reproduce the observed dramatic changes in the chloride (open circles) and gas hydrate distributions observed at Site 1249, and reach the observed conditions in less than 1500 years.

correspond to a gas hydrate occupancy of $\sim 15\%$ of the pore space. In the second case (broken lines in Fig. 8A), k_G^{B} and k_G^{MAX} were set to 10^{-3} and 0.4 year^{-1} , and again using a flow velocity of 1 cm year^{-1} , the model requires 1000 years to develop the measured chloride values, during which time gas hydrate

occupancy reaches 20% vol. In both cases, the resulting model curves reproduce the abrupt change in the dissolved chloride and gas hydrate distributions observed in the upper reaches of the sediments at the summit of Hydrate Ridge.

Alternatively, in scenario 3B we allowed for changes with depth in the kinetic constant for gas hydrate formation, following a Boltzmann function:

$$k_H = 0.00001 + [0.01 - 0.00001] / [1 + \exp(z - 10)/3] \quad (20)$$

This function results in k_H values close to 0.01 over the top 20 m of the sediment column, decaying to a value of 10^{-5} at the base of the column. The results of this scenario using a fluid advection rate of 1 cm/year^{-1} are shown in Fig. 8B. The solid lines show the results after an integration time of 1500 years, using a kinetic constant for gas dissolution $k_G=0.1 \text{ year}^{-1}$, and the broken lines illustrate the results after 150 years, using $k_G=1 \text{ year}^{-1}$. This scenario also predicts the development of a brine with dissolved chloride concentrations that reproduced the measured values. The gas hydrate content of the sediments reaches 25% vol. in near surface sediments, and decreases abruptly below 20 mbsf, also consistent with observations of the gas hydrate distribution.

3.7. Justification for varying kinetic constants with depth

Sediment geomechanical properties are known to affect both bubble and gas hydrate dynamics [41–43]. In deformable shallow sediments, the gas pressure can overcome the effective stress of the surrounding sediment, leading to the formation of bubbles in which the bubble cavity is larger than the normal sediment interstitial space. The sediment is thus distorted by cavity expansion due to gas exsolution. Indirect evidence was used to postulate the presence of gas bubbles larger than normal void spaces (e.g., [1,44]). Such bubbles were indeed observed by X-ray CT scanning of sediments recovered at in situ pressure from the muddy sediments of Eckernförde Bay, Germany [42]. As depth increases, matrix stresses will force the bubbles to distort and eventually collapse [40,43].

Clennell et al. [7] describe and quantify the inhibiting effects of capillary pressures in the formation of bubbles and hydrate. Both bubbles and hydrate will grow within porous media until all pore throats greater than a critical size have been penetrated. After this, any further growth must occur by displacing sediment grains. This process is analogous to ice formation in soils, as described in [44], where growing crystals can push away soil particles, resulting in frost heave damage. Grain displacement can occur only when either gas or hydrate phase pressure can overcome the effective confining stress (σ_e) plus the tensile strength of the sediment (E_s), as given by the relationships:

$$P_h > \sigma_e + E_s \quad (21)$$

$$P_g > \sigma_e + E_s \quad (22)$$

where P_h and P_g represent the phase pressure of hydrate and gas (Table 2).

The effective stress increases with depth, and may be estimated by the relationship:

$$\sigma_e = gz(\rho_{\text{bulk}} - \rho_{\text{pw}}) \quad (23)$$

where ρ_{bulk} is the integrated wet bulk density of all overlying sediments, and g is the gravitational force. Changes in effective confining stress with depth calculated using wet bulk density data from Site 1249 [27] are shown in Fig. 9, which includes the values for the internal gas and hydrate pressures (P_h and P_g) estimated for a hydrate crystallite and gas bubble, both with a radius of $0.5 \mu\text{m}$ [27,7]. Using these approximations, Fig. 9 shows that the internal pressures of gas and hydrate crystallites will exceed the effective stress at depths of 39 and 19 mbsf, respectively. This depth range roughly corresponds to that of the onset of massive hydrate and chloride brine at the Hydrate Ridge summit.

We envision a system where restricted hydrate and bubble growth in clays and silts at depths >20 mbsf require a progressively greater methane supersaturation

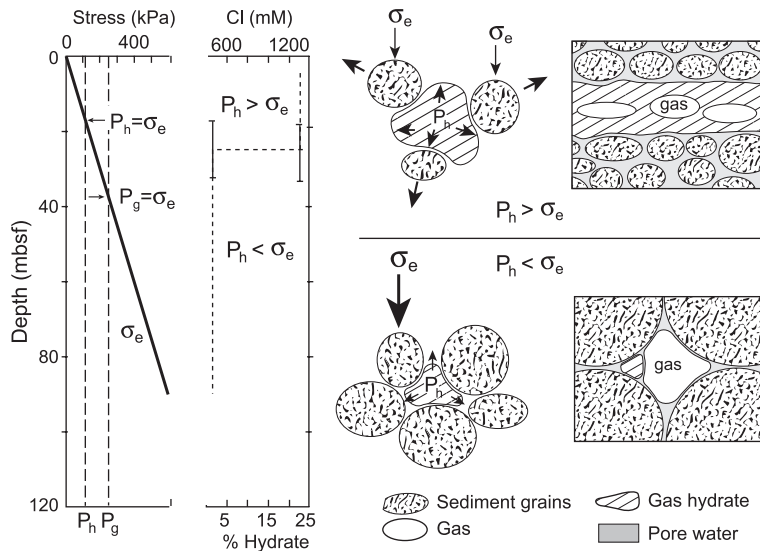


Fig. 9. Schematic representation of the effect of geomechanical and physical properties of the sediment on gas hydrate and bubble textures. Left panel illustrates the increase in effective overburden stress (σ_e) with depth. The internal pressures of hydrate crystallite (P_h) and gas bubbles (P_g) were estimated using the relationships of Clennell et al. [7], assuming an average pore radius of $0.5 \mu\text{m}$ for the silty-clay sediment at this site [27]. The effective overburden stress intercepts the internal pressures of hydrate and gas at 19 and 39 mbsf, respectively. Above 20 mbsf, internal pressures are large enough to push aside the sediment grains (upper-right panels, redrawn from [7]), and result in enhanced gas hydrate contents and brine formation in these sediments. Deeper than 20 mbsf $P_g > P_h$, thus the effective overburden stress inhibits gas hydrate formation as shown by Clennell et al. [7] (lower-right panels).

in order for the crystals and bubbles to adopt greater surface curvatures as smaller throats are penetrated. At ~ 20 mbsf, the bubble and hydrate pressures will exceed the overburden effective stress and push away sediment particles to form bubbles and crystals larger than the available pore spaces. Conceptually, this is equivalent to minimizing the time needed for transfer of methane to the dissolved phase from which the hydrate is forming, thus the rationale for our scenario 3A. Alternatively, the increase in effective overburden stress with depth may simply inhibit gas hydrate formation at depth, as modeled in scenario 3B.

4. Comparison with other results

We recognize that our one-dimensional vertical transport model, though internally consistent, represents a simplified look at the gas transport on Hydrate Ridge and that more structure and complexity is indeed present. Hydrocarbon analyses by Milkov et al. [45] revealed that gas migration at the ridge summit does not follow a simple vertical path. They postulate that gas rises through the GHSZ beneath a carbonate structure known as the Pinnacle (Fig. 10), followed by lateral migration to the crest in the upper tens of meters below seafloor [18,45]. On the other hand, Tréhu et al. [46] have shown that the gas pressure beneath the BSR may be high enough to initiate and sustain steady-state gas migration to the seafloor over a broader region, suggesting that upward methane transport occurs via a random network of gas-filled capillaries across the summit (Fig. 10).

The methane gas discharge at the seafloor on southern Hydrate Ridge has been previously estimated to be $\sim 10^4$ mol day $^{-1}$ [35]. In addition, independent calculations suggest that $\sim 10^{10}$ mol of methane is trapped in hydrate within the upper 30 m of sediment at the summit, covering an area of $\sim 1.5 \times 10^5$ m 2 [24] (Table 4). If we assume that the system has reached steady state, methane release at the seafloor must be equal to that delivered at the base of the GHSZ. Using this assumption and the results of [11,24,35], the rate of supply of methane is enough to form the total amount of hydrate currently present in the summit of Hydrate Ridge in a time scale of 500 years. These values agree with our model predictions, which although highly uncertain, indicate formation of the gas hydrate

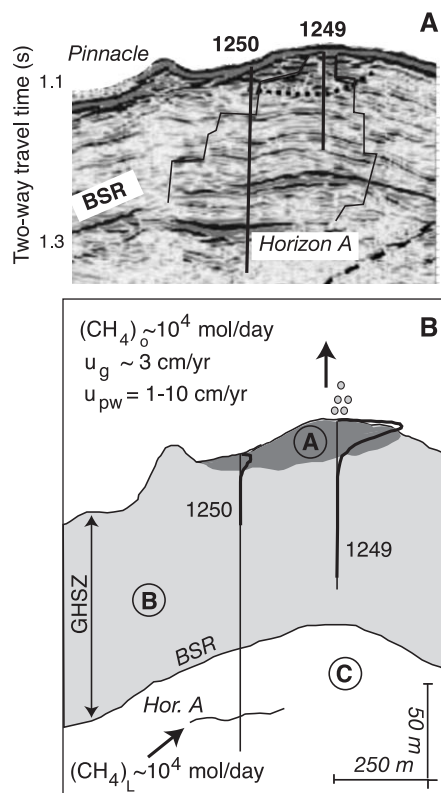


Fig. 10. (A) Section from 3D-Seismic data near the summit of southern Hydrate Ridge showing two possible paths of gas migration to the summit (from [46]). (B) Schematic representation of the gas hydrate forming system at the southern summit of Hydrate Ridge. The topographic high west of the summit is a porous carbonate edifice known as “Pinnacle”, which has been dated as 7–11 ka [50]. The location and depth of penetration of Sites 1249 and 1250 are depicted by solid lines, on which we have superimposed schematic dissolved chloride profiles showing the depth extent of the brine. Methane, hydrate and chloride distributions in zones A, B and C are detailed in Table 4. Dark area demarcated as A corresponds to the zone of high-amplitude, chaotic reflectivity in the 3D-seismic data. The lateral extent of this seismic pattern ($\sim 15 \times 10^4$ m 2) is coincident with moderate-to-high seafloor acoustic backscatter [17]. Methane discharge at the ridge summit has been estimated to be $\sim 10^4$ mol/day [11,37]. GHSZ= gas hydrate stability zone. $(\text{CH}_4)_O$ and $(\text{CH}_4)_L$ are the methane fluxes at the seafloor and the base of GHSZ, respectively.

deposits and associated brine in less than 1500 years (Table 3).

Using these first-order estimates, the rates of hydrate formation at the ridge crest are in the order of 10^2 mol CH $_4$ m $^{-2}$ year $^{-1}$, which is at least five orders of magnitude faster than that estimated for Site 997 on the Blake Ridge ($\sim 5 \times 10^{-4}$ mol CH $_4$ m $^{-2}$

Table 4
Summary of methane and chloride distributions in Zones A, B and C from Fig. 10

	Depth range at site 1249 (mbsf)	Depth range at site 1250 (mbsf)	Hydrate concentration (vol.%) [24]	Hydrate distribution	Dissolved methane (mM)	Dissolved chloride (mM)
Zone A	0 to ~25	0 to ~15	20–30	Massive, forms by sediment displacement (Fig. 9). Total methane trapped in hydrate $\sim 10^{10}$ mol [24].	At saturation values from ~25 to 3.5 mbsf. At shallow depths, dissolved methane decreases by diffusion to bottom seawater.	Brine, maximum measured value of 1370 mM.
Zone B	~25 to 115	~15 to 112	Averages 2–5	Heterogeneous, preferentially associated with coarse layers and small faults.	Likely to be supersaturated due to capillary inhibition of bubble and hydrate formation.	Background near seawater values, with discrete negative anomalies associated with hydrate layers.
Zone C	>115	>112	Below GHSZ, no gas hydrate. Methane transport via coarse sediment layer known as Horizon A [49].			Near seawater values.

year⁻¹, [33]). Extremely high rates of hydrate formation have also been postulated based on oxygen and hydrogen isotope data from the ridge summit

[47]. The extreme rates of gas hydrate formation in near surface sediments of Hydrate Ridge can explain the presence of bubbles trapped within the gas hydrate

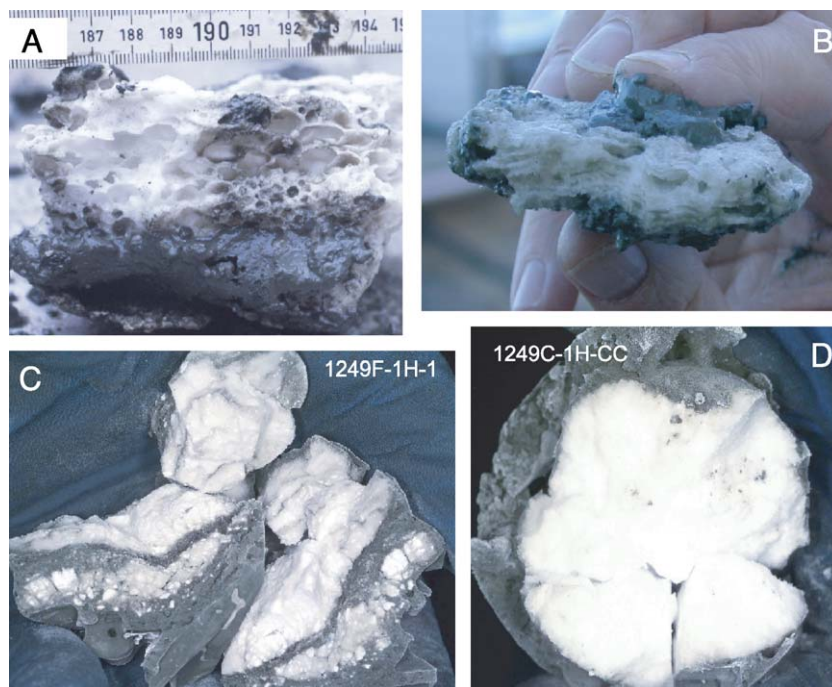


Fig. 11. (A–B) Gas hydrate samples collected near the seafloor with a TV-guided grab reveal the presence of macroscopic bubbles [48]. This fabric is consistent with very rapid growth at negligible confining pressures. (C–D) Illustrates massive hydrate deposits recovered in the upper 30 mbsf by drilling in Zone A ($z > 1$ mbsf) do not show macroscopic bubble entrapment. Either the gas rate of formation at these depths is slower than those at the seafloor or there has been redistribution of the hydrate structure towards a more compact form as demonstrated experimentally by Tohidi et al. [39].

fabric recovered from the seafloor (Fig. 11, [48]). Visual observations of experimental gas hydrate formation document crystallization from free methane at the gas–water interface, encapsulating bubbles in a crust of gas hydrate [39]. The hydrate crust was observed to collapse inward as hydrate regions grow in size by the agglomeration of smaller crystals, as required to minimize surface area and energy [39]. Gas hydrate samples recovered deeper within the sediments at the summit of Hydrate Ridge show no evidence of macroscopic bubbles (Fig. 11), which suggest that even if large bubbles were originally trapped within the hydrate structure, it has since collapsed into a more compact form.

We integrate this information in a simplified scheme for the formation of massive hydrate deposits at the ridge summit. Approximately 10^4 mol of methane is delivered per day to the base of the GHSZ, likely by free gas transport through the high permeability path imaged seismically as Horizon A [10,46]. Gas and water migrate upward towards the summit. Water flow velocities may be less than 1 cm year^{-1} , and at most 10 cm year^{-1} . The gas advection rate (corresponding to a discharge rate $10^4 \text{ mol day}^{-1}$ over an area of $\sim 1.5 \times 10^5 \text{ m}^2$) is $\sim 3 \text{ cm year}^{-1}$. Gas flow probably occurs either by catenary transport or invasion-percolation [40,49] in a random network of gas-filled capillaries [46]. These are not concentrated directly underneath the drilled sites as evidenced by hydrocarbon analyses [45], but eventually vent at the ridge crest [13]. Gas transport through the GHSZ results in gas hydrate formation, which is enhanced in the upper 20 mbsf where the overburden stress is less than the internal pressures of growing hydrate crystals and gas bubbles (Fig. 9). The gas supply sequesters methane as hydrate in the upper sediments on the summit (Zone A, Fig. 10) at a rate of $\sim 10^2 \text{ mol m}^{-2} \text{ year}^{-1}$.

Dating of carbonate deposits from the Pinnacle yields ages of 7–11 ka [50], suggesting that the system has been active for at least 7000 years. Various data [11,24,35] discussed above indicate that the massive deposit at the summit ($\sim 10^{10} \text{ mol CH}_4$) was formed in less than 1500 years. Further growth of the hydrate was probably constrained by development of highly saline fluids [18], although a dynamic equilibrium requires that the near-surface hydrate forms constantly in order to replace the salinity lost by continuous diffusion to the bottom water. Loss of salts will shift the thermody-

namic equilibrium to allow for more hydrate formation, and some of this hydrate will dissolve when equilibrium salinity is reestablished. In addition, a periodic release of methane slabs from the seafloor may be triggered by the strong positive buoyancy force of these deposits [20,26]. As the hydrate buoyancy overcomes the shear strength of the host sediment, methane hydrate is released. This process leaves behind the unusual seafloor topography of mounds and depressions observed on the southern ridge summit [11].

5. Conclusions

1. The massive gas hydrate deposits, which coexist with highly saline pore fluids at the summit of Hydrate Ridge, cannot be formed by upward transport of methane solely in the dissolved phase due to the low methane solubility. Transport of methane as a free gas phase within the GHSZ is necessary to sustain the observed methane hydrate deposits and chloride enrichment in the pore fluids. The presence of free gas within the GHSZ is supported by geophysical data and observations of gas vents. Critically pressured free gas beneath the GHSZ provides a driving force for gas migration [46].
2. The observed gas hydrate and chloride distributions, which decrease abruptly beneath 25 ± 5 mbsf, are driven primarily by a decrease in effective overburden stress in near surface sediments. Massive hydrate deposits, such as those present near the seafloor on Hydrate Ridge and elsewhere, require transport of methane gas at least to the depth where bubble pressure exceeds the effective overburden stress.
3. First order estimates of the methane gas flux based on seafloor and water column observations at this site [11,35] indicate that the supply rates at the bottom of the GHSZ are enough to generate the massive hydrate deposits in a time scale of ~ 500 years, consistent with our model results. Methane hydrate here precipitates at extremely fast rates ($\sim 10^2 \text{ mol CH}_4 \text{ m}^{-2} \text{ year}^{-1}$), consistent with gas hydrate texture [39,48] and water isotope data [47]. These rates are several orders of magnitude higher than those estimated for gas hydrate formation on the Blake Ridge [33].

Acknowledgements

This research used data provided by the Ocean Drilling Program (ODP), which is sponsored by the US National Science Foundation (NSF) and participating countries under management of Joint Oceanographic Institutions (JOI), Inc. Funding for this research was provided by the US Science Support Program (USSP), and the German Ministry of Research and Education within the Geotechnology Program (LOTUS and OMEGA). We thank the captain and crew of the *JOIDES Resolution* and the ODP technical staff for their stellar support at sea. We want to acknowledge Dennis Graham and W. Brian Jones for their extremely valuable assistance in the chemistry laboratory and M. Hovland, R. Hesse and A. Milkov for comments to this manuscript.

References

- [1] M. Hovland, A.G. Judd (Eds.), *Seabed Pockmarks and Seepages: Impact on Geology, Biology and the Marine Environment*, Graham and Trotman, London, 1998, 293 pp.
- [2] G.R. Dickens, Rethinking the global carbon cycle with a large, dynamic and microbially mediated gas hydrate capacitor, *Earth Planet. Sci. Lett.* 213 (2003) 169–183.
- [3] D.E. Sloan Jr., *Clathrate Hydrates of Natural Gases*, Second edition, Marcel Dekker, New York, 1998, revised and expanded, 705 pp.
- [4] R. Hesse, Pore water anomalies of submarine gas-hydrate zones as a tool to assess hydrate abundance and distribution in the subsurface. What have we learned in the past decade? *Earth Sci. Rev.* 61 (2003) 149–179.
- [5] G.R. Dickens, M.S. Quinby-Hunt, Methane hydrate stability in pore water: a simple theoretical approach for geophysical applications, *J. Geophys. Res.* 102 (1997) 773–783.
- [6] O.Y. Zatsepina, B.A. Buffett, Phase equilibrium of gas hydrate: implications for gas hydrate formation in the deep seafloor, *Geophys. Res. Lett.* 24 (1997) 1567–1570.
- [7] M.B. Clennell, A. Judd, M. Hovland, Movement and accumulation of methane in marine sediments: relation to gas hydrate systems, in: M.D. Max (Ed.), *Natural Gas Hydrate in Oceanic and Permafrost Environments*, Kluwer Academic Publishers, The Netherlands, 2000, pp. 105–122.
- [8] K.A. Kvenvolden, T.D. Lorenson, The global occurrence of natural gas hydrate, in: C.K. Paull, W.P. Dillon (Eds.), *Natural Gas Hydrates Occurrence, Distribution, and Detection*, Geophysical Monographs, vol. 124, American Geophysical Union, Washington, DC, 2001, pp. 3–18.
- [9] A. Milkov, G. Claypool, Y.-J. Lee, W. Xu, G.R. Dickens, W.S. Borowski, ODP Leg 204 scientific party, In situ methane concentrations at hydrate ridge, offshore Oregon: new constraints on the global gas hydrate inventory from an active margin, *Geology* 31 (2003) 833–836.
- [10] A.M. Tréhu, G. Bohrmann, F. Rack, M.E. Torres, et al., Proc. ODP, Init. Repts. 204 (2003)[Online]. http://www-odp.tamu.edu/publications/204_IR/204ir.htm.
- [11] M.E. Torres, J. McManus, et al., Fluid and chemical fluxes in and out of sediments hosting methane hydrate deposits on Hydrate Ridge, OR: I. Hydrological provinces, *Earth Planet. Sci. Lett.* 201 (2002) 525–540.
- [12] M.D. Tryon, K.M. Brown, M.E. Torres, Fluid and chemical fluxes in and out of sediments hosting hydrate deposits on Hydrate Ridge, OR, II: observations and long-term records reveal insights into dynamic driving mechanisms, *Earth Planet. Sci. Lett.* 201 (2002) 541–557.
- [13] K.U. Heeschen, A.M. Tréhu, R.W. Collier, E. Suess, G. Rehder, Distribution and height of methane bubble plumes on the Cascadia margin characterized by acoustic imaging, *Geophys. Res. Lett.* 30 (2003) 1643–1646.
- [14] E. Suess, M.E. Torres, G. Bohrmann, R.W. Collier, J. Greinert, P. Linke, G. Rehder, A. Tréhu, K. Wallmann, G. Winckler, E. Zuleger, Gas hydrate destabilization: enhanced dewatering, benthic material turnover and large methane plumes at the Cascadia convergent margin, *Earth Planet. Sci. Lett.* 170 (1999) 1–15.
- [15] A.M. Tréhu, N.L. Bangs, M.A. Arsenault, G. Bohrmann, C. Goldfinger, J.E. Johnson, Y. Nakamura, M.E. Torres, Complex subsurface plumbing beneath Southern Hydrate Ridge, Oregon continental margin, from high resolution 3D seismic reflection data, Fourth Intern. Conf. Gas Hydrates, Yokohama, Japan, 2002, pp. 90–96.
- [16] D. Clague, N. Maher, C.K. Paull, High resolution multibeam survey of Hydrate Ridge, offshore Oregon, in: C.K. Paull, W.P. Dillon (Eds.), *Natural Hydrates: Occurrence, Distribution and Detection*, Am. Geophys. Union, Geophys. Monogr. Ser., vol. 124, 2001, pp. 297–306.
- [17] J.E. Johnson, C. Goldfinger, E. Suess, Geophysical constraints on the surface distribution of authigenic carbonates across the Hydrate Ridge region, Cascadia margin, *Mar. Geol.* 202 (2003) 79–120.
- [18] A. Milkov, G.R. Dickens, G.E. Claypool, Y.-J. Lee, W. Borowski, M.E. Torres, W. Xu, H. Tomaru, A. Tréhu, P. Schultheiss, Leg 204 Scientific party, Co-existence of free gas, gas hydrate and brine within the gas hydrate stability zone at the southern summit of Hydrate Ridge (Oregon margin): evidence from prolonged degassing of a pressurized core, *Earth Planet. Sci. Lett.* 222 (2004) 829–843.
- [19] F. Abegg, J. Freitag, G. Bohrmann, W. Brueckmann, A. Eisenhauer, H. Aman, H.-J. Hohnberg, Free gas bubbles in the hydrate stability zone: evidence from CT investigation under in situ conditions. Spring 2003 abstract #EAE-A-10342, AGU meeting, Nice, France.
- [20] E. Suess, M.E. Torres, et al., Sea floor methane hydrates at Hydrate Ridge, Cascadia margin, in: C.K. Paull, W.P. Dillon (Eds.), *Natural Gas Hydrates: Occurrence, Distribution, and Detection*, Am. Geophysical Union, Geophys. Monogr. Ser., vol. 124, 2001, pp. 87–98.

- [21] A.R. Gorman, W.S. Holbrook, M.J. Hornbach, K.L. Hackwith, D. Lizarralde, I. Pecher, Migration of methane gas through the hydrate stability zone in a low flux hydrate province, *Geology* 30 (2002) 327–330.
- [22] P.B. Flemings, X. Liu, W. Winters, Critical pressure and multiphase fluid flow in Blake Ridge gas hydrates, *Geology* 31 (2003) 1057–1060.
- [23] W. Ussler, C.K. Paull, Ion exclusion associated with marine gas hydrate deposits, in: C.K. Paull, W.P. Dillon (Eds.), *Natural Gas Hydrates: Occurrence, Distribution, and Detection*, American Geophysical Union, Geophysical Monographs, vol. 124, 2001, pp. 41–51.
- [24] A.M. Tréhu, P.E. Long, M.E. Torres, et al., Three-dimensional distribution of gas hydrate beneath southern Hydrate Ridge: constraints from ODP Leg 204, *Earth Planet. Sci. Lett.* 222 (2004) 845–862.
- [25] J. Gieskes, T. Gamo, H.-J. Brumsack, Chemical methods for interstitial water analysis aboard JOIDES Resolution, ODP Tech. Note, 15, College Station TX, 1991, [Online]. http://www-odp.tamu.edu/publications/tnotes/tn15/f_chem1.htm.
- [26] E. Suess, G. Bohrmann, D. Rickert, W. Kuhs, M. Torres, A. Tréhu, P. Linke, Properties and fabric of near-surface hydrates at Hydrate Ridge, Cascadia margin, Fourth Intern. Conf. Gas Hydrates, Yokohama, Japan, 2002, pp. 740–744.
- [27] Shipboard Scientific Party, Site 1249. In: Tréhu, A.M., Bohrmann, G., Rack, F.R. Torres, M.E. et al., *Proc. ODP Init. Repts. 204* (2003) 1–132 [CD-ROM]. Available from: Ocean Drilling Program, Texas A and M University, College Station, TX 77845-9547-USA, [Online]. http://www-odp.tamu.edu/publications/204_IR/204ir.htm.
- [28] B.P. Boudreau, *Diagenetic Models and Their Implementation: Modelling Transport and Reactions in Aquatic Systems*, Springer-Verlag, 1997, 414 pp.
- [29] R.A. Berner, *Early Diagenesis: A Theoretical Approach*, Princeton Univ. Press, Princeton, NJ, 1980, 241 pp.
- [30] A.M. Tréhu, E. Dillard III, J. Huckemeyer, D. Schoeder, Leg 204 Science Party, In situ temperature and thermal conductivity beneath Southern Hydrate Ridge. Leg 204 (abs.), Spring 2003 AGU meeting, Nice, France, 2003, EAE03-A-07296.
- [31] D. Turcotte, G. Schubert, *Geodynamics, Applications of Continuum Physics to Geological Problems*, 2002, 456 pp.
- [32] P. Tishchenko, C. Hensen, K. Wallmann, C. Peng, The stability and solubility of methane hydrate in seawater, *Earth Planet. Sci. Lett.* (2003) (in review).
- [33] P.K. Egberg, G.R. Dickens, Thermodynamic and pore water halogen constraints on gas hydrate distribution at ODP Site 997 (Blake Ridge), *Chem. Geol.* 153 (1999) 53–79.
- [34] A.C. Lasaga, *Kinetic Theory in the Earth Sciences*, Princeton University, Princeton, NJ, 1981, 811 pp.
- [35] K.U. Heeschen, R.W. Collier, M.A. DeAngelis, E. Suess, G. Rehder, P. Linke, G.P. Klinkhammer, Methane sources, distributions, and fluxes from cold vent sites at Hydrate Ridge, Cascadia Margin, *Glob. Biogeochem. Cycles* (2004) (submitted for publication).
- [36] A.W. Rempel, B.A. Buffett, Mathematical models of gas hydrate accumulation, *Gas Hydrates: Relev. World Margin Stab. Clim. Change* 137 (1998) 63–74.
- [37] M.K. Davie, B.A. Buffett, A numerical model for the formation of gas hydrate below the seafloor, *J. Geophys. Res.* 106 (2001) 497–514.
- [38] P.G. Brewer, F.M. Orr Jr., G. Friederich, K.A. Kvenvolden, D.L. Orange, J. McFarlane, W. Kirkwood, Deep-ocean field test of methane hydrate formation from a remotely operated vehicle, *Geology* 25 (1997) 407–410.
- [39] B. Tohidi, R. Anderson, A.B. Biderkab, R.W. Burgass, M.B. Clennell, Visual observation of gas-hydrate formation and dissociation in synthetic porous media by means of glass micromodels, *Geol. Soc. Am. Geol.* 29 (2001) 867–870.
- [40] M.B. Clennell, M. Hovland, J.S. Booth, P. Henry, W.J. Winters, Formation of natural gas hydrates in marine sediments 1. Conceptual model of gas hydrate growth conditioned by host sediment properties, *J. Geophys. Res.* 104 (1999) 22985–23003.
- [41] S.J. Wheeler, Movement of large gas bubbles in unsaturated fine-grained sediments, *Mar. Geotechnol.* 9 (1990) 113–129.
- [42] A.L. Anderson, F. Abegg, J.A. Hawkins, M.E. Duncan, A.P. Lyons, Bubble populations and acoustic interaction with the gassy seafloor of Eckernförde Bay, *Cont. Shelf Res.* 18 (1998) 1807–1838.
- [43] G.C. Sills, S.J. Wheeler, S.D. Thomas, T.N. Gardner, Behavior of offshore soils containing gas bubbles, *Geotechnique* 41 (1991) 227–241.
- [44] G.W. Scherer, Freezing gels, *J. Non-Cryst. Solids* 155 (1993) 1–25.
- [45] A.V. Milkov, G.E. Claypool, Y.-J. Lee, R. Sassen, Gas hydrate systems at Hydrate Ridge offshore Oregon inferred from molecular and isotopic properties of hydrate-bound gases, *Geochim. Cosmochim. Acta* (2004) (in review).
- [46] A.M. Tréhu, P. Flemings, N. Bangs, E. Gracia, C.-S. Liu, M. Riedel, J. Chevallier, J.E. Johnson, M.E. Torres, Critically pressured free-gas and venting at South Hydrate Ridge, Cascadia accretionary complex, *Geology* (2004) (in review).
- [47] H. Tomaru, R. Matsumoto, M.E. Torres, W. Borowski, Leg 204 Science Party, Fluid migration and formation of massive gas hydrates in Hydrate Ridge, Cascadia continental margin, Geochemical indications by chloride concentrations and oxygen-hydrogen isotopic compositions 32nd International Geological Congress, Florence, Italy, 2004.
- [48] G. Bohrmann, E. Suess, J. Greinert, B. Teichert, T. Naeher, Gas hydrate carbonates from Hydrate Ridge, Cascadia convergent margin: indicators of near seafloor chlathrate deposits, Fourth Intern. Conf. Gas Hydrates, Yokohama, Japan, 2002, pp. 102–107.
- [49] M.D. Impey, P. Grindrod, H. Takase, K.J. Worgan, A capillary network model for gas migration in low-permeability media, *SIAM J. Appl. Math.* 57 (1997) 597–608.
- [50] B.M.A. Teichert, A. Eisenhauer, A. Haase-Schramm, B. Bock, P. Linke, U/Th systematics and ages of authigenic carbonates from Hydrate Ridge, Cascadia convergent margin: recorders of fluid composition and sealevel changes, *Geochim. Cosmochim. Acta* 67 (20) (2003) 3845–3857.